HIGH DENSITY COMPRESSION OF HOLLOW PELLET BY GEKKO XII AT OSAKA

T. YAMANAKA, S. NAKAI, K. MIMA, Y. IZAWA, Y. KATO, K. NISHIHARA, T. SASAKI, M. NAKATSUKA, M. YAMANAKA, H. AZECHI, T. JITSUNO, T. NORIMATUS, K. A. TANAKA, N. MIYANAGA, M. NAKAI, M. TAKAGI, M. KATAYAMA, H. NAKAISHI, and Y. SETSUHARA

Institute of Laser Engineering, Osaka University, 2–6 Yamada-oka, Suita, Osaka 565, Japan

and

A. NISHIGUCHI, T. KANABE and C. YAMANAKA

Institute for Laser Technology, 2–6 Yamada-oka, Suita, Osaka 565, Japan.

Direct-drive implosion experiments on the Gekko XII laser demonstrated high density compression needed for thermonuclear ignition and burning. Deuterated and tritiated plastic hollow shell targets, which are similar design of cryogenic DT shell targets, were compressed up to 600 g/cm^3. The plasma was verified to be a partial Fermi degenerated plasma. Those results were owed to the improvements of laser illumination uniformity by introducing a random phase plate, target quality and neutron activation technique for areal density diagnostics.

1 INTRODUCTION

It has long been quoted that for inertial confinement fusion (ICF) one needs to compress thermonuclear fusion fuel up to 500 ~ 1,000 times of solid density (SD) and then heat up the target center (hot spark) enough to burn the remainder of the fuel. Some implosion experiments[1] show favorable results concerning hot spark formation. However the reported density[2-4] is only 100 ~ 200 × SD and well below the required value for thermonuclear ignition and burning.

We have demonstrated 600 × SD, which almost meets the density criterion for ICF, and verified the plasma to be partially Fermi degenerated. Those results are owed to improvements in target quality, laser illumination uniformity and diagnostic techniques.

Instead of a cryogenically cooled DT solid/liquid target, a deuterated and tritiated plastic-shell target (CDT) is used in order to study implosion properties of a spherical shell target, since its quality is much better than that of the present cryogenic targets and thus experiments can be performed that are not limited by present cryogenic

target technology. In addition, the initial density of the fuel atoms (D and T) in the plastics is approximately equal to the DT liquid density. In the area of lasers, the energy imbalance of the twelve beams of Gekko XII was reduced, with a standard deviation as small as 1%. The target illumination nonuniformity was improved to be as small as 14% rms for a 500 μm diameter target by introducing a random phase plate. A major improvement in diagnostics is the establishment of a neutron activation technique valid for $\rho R > 100$ mg/cm^2.

2   EXPERIMENTAL CONDITIONS

The experiments were performed using the Gekko XII 12-beam glass laser (Figure 1). The wavelength is upconverted to 0.53 μm. The laser energy at 0.53 μm was 8–10 kJ with a 1 ns Gaussian pulse in full width at half maximum (FWHM) or with a flat-top pulse having a nominal width of 1.7 ns and a risetime equivalent to a 1–1.3 ns Gaussian pulse. The beam energy imbalance was controlled to be $\sim 1\%$ in standard deviation. The laser illumination uniformity was improved by introducing a random phase plate (RPP)[5] in front of each focusing lens. The random phase plate divided a 35 cm-diameter single laser beam into $\sim 20\,000$ beamlets, each of which has a 2 $\times$ 2 mm cross section, producing a focal pattern that has a smooth envelope
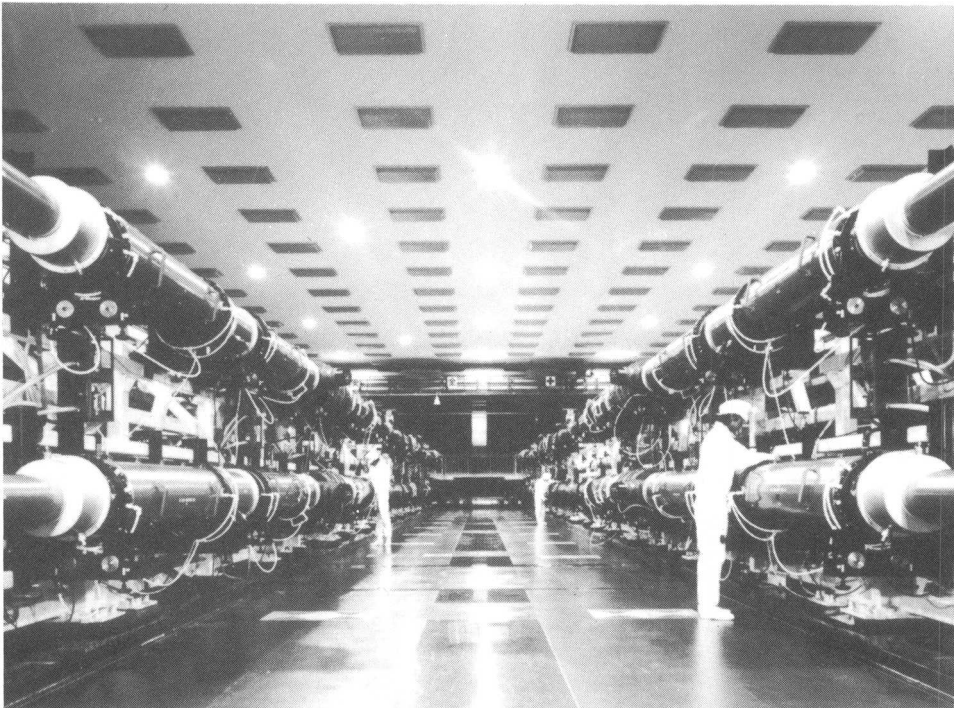

FIGURE 1   Gekko XII 12-beam glass laser. The output energy in 1 ns at 1 μm wavelength, is 30 kJ.

(with small-scale spikes due to the interference between the beamlets). The intensity distribution on a spherical target was calculated with the measured data on the target plane as a function of spherical harmonic mode number. The rms nonuniformity with the RPP was found to be 14% for the nominal 500 μm-diameter target as shown in Figure 2. Assuming that the distance d between the cut-off density and ablation surfaces is 5% of the initial target radius, the nonuniformity is improved to be 4.6% due to the thermal smoothing effect. The 1-d hydrodynamic code HIMICO[6] predicted larger d except for the very early initial period of the laser pulse. However, we used the value above as a conservative assumption. The fraction of laser energy launched on a 500 μm diameter target was calculated to be 65% of the incident energy for the RPP case.

As for the fabrication of plastic shell targets technique we used an improved water/oil/water (W/O/W) emulsion method[7] in which the specific gravity of the oil phase was matched with that of the water phase in order to eliminate troublesome gravitational effects. As a result, both the nonsphericity and the nonuniformity of the target thickness were controlled to be $\sim 1\%$. A deuterated-styrene and deuterated-para-trimethylsilylstyrene copolymer $[(C_8D_8)_n - (C_{11}D_{16}Si)_m]$ was used to prepare the Si-doped plastic shells. Si atoms are used as a tracer for the diagnostics described below. The amount of Si was controlled to be 5–15% by weight by changing the n/m ratio. The mass densities of plastic and of deuterium included in it were 1 and 0.15–0.17 g/cm^3, respectively. Some of deuterium in the targets was exchanged with tritium[8], giving tritium-to-deuterium ratios of 3 $\sim$ 10%.
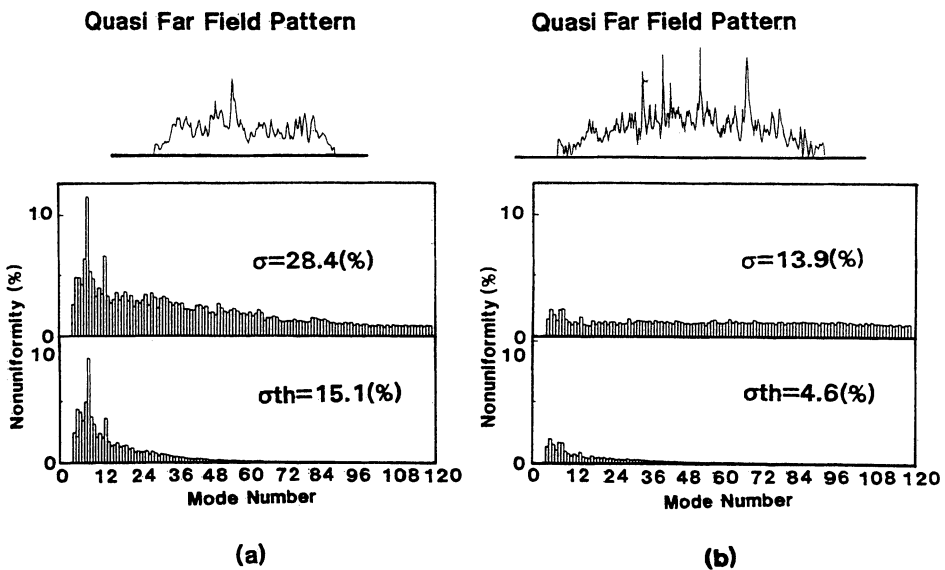

FIGURE 2 Laser illumination nonuniformity as a function of spherical harmonic mode number, and quasi-far-field pattern. (a) Normal beam; (b) With random phase plate. Focusing condition; $d/R = -5$, target diameter 500 μm. Upper data show the nonuniformity at initial target surface. Lower data include the thermal smoothing effect.

As for fuel $\langle \rho R \rangle$ measurements, three independent techniques were used: secondary reaction[9], knock-on deuteron[10] or proton[11], and neutron activation[12] techniques. The secondary reaction and knock-on techniques, however, have an upper limit on their measurable $\langle \rho R \rangle$ values, above which primary 1-MeV tritons or knock-on particles slow down significantly in the fuel. We, therefore, adopted neutron activation technique for $\langle \rho R \rangle$ measurements since it has practically no $\langle \rho R \rangle$ limitation. The other techniques were used for cross-examination.

Si was selected as a tracer atom for the neutron activation method. The activation reaction is $^{28}Si(n, p)^{28}Al$, having a cross section of 0.26 barns for 14-MeV neutrons. The ratio of the number of ^{28}Al to the neutron yield is directly proportional to the fuel $\langle \rho R \rangle$. The ^{28}Al atom decays back to ^{28}Si, producing β and γ rays simultaneously with a half life of 2.24 min and a distinct γ-energy of 1.78 MeV.

The counting system of ^{28}Al decay consisted of a gas flow counter for β-ray detection and an NaI scintillation counter for γ-ray detection. The detection efficiency of β–γ coincidence events was absolutely calibrated to be 4%. The γ-ray spectra and its decay constant were measured using a β–γ coincidence technique. The debris collector used in these experiments was an Nb cylinder of 4.4 cm diameter and 10 cm length. The collector covered 85% of the total 4π solid angle, both to increase signal counts and to eliminate unwanted effects due to possible angular distribution of the debris expansion. The debris collection efficiency was calibrated, using pre-activated targets containing Na, and was found to be 38% with a shot-to-shot fluctuation of $\pm 3\%$. It was assumed that the Na collection efficiency was the same as the Al collection efficiency. This assumption was justified by the very good agreement of the fuel $\langle \rho R \rangle$ values measured with both Si activation and knock-on deuteron techniques simultaneously[13].

The DT neutron yields (Y_n) due to the secondary nuclear reaction were measured with two time-of flight detectors, each of which consisted of a plastic scintillator coupled to a photomultiplier. In the target shots yielding about 10^6 DT neutrons (typical yield in the high-density experiments), about 500 recoil events in each detector can be anticipated and the uncertainties involved in the statistical number are insignificant. This neutron yield was examined to be reasonable for the measured ρR, ρ, and temperature. In the present experiments in which the targets contain only small amount of tritium, DT neutron yield is comparable to DD neutron yield, which might affect the accuracy of the yield measurements. However the time-of-flight difference makes the contribution of DD neutrons to the DT neutron yield measurement insignificant. These time-of-flight detectors were absolutely calibrated in several high yield shots, where Y_n was simultaneously measured with Al and Si activation techniques. The uncertainty of Y_n measurement is estimated to be $\pm 15\%$.

3   EXPERIMENTAL RESULTS

3.1   High Density Compression

Typically 40% of the laser energy (65% of the laser energy incident on the targets) was absorbed on the targets in the laser illumination condition of $d/R_0 = 5$, where R_0 is target radius and d is distance between target center and focal point.

Imploding   Maximum   Expanding
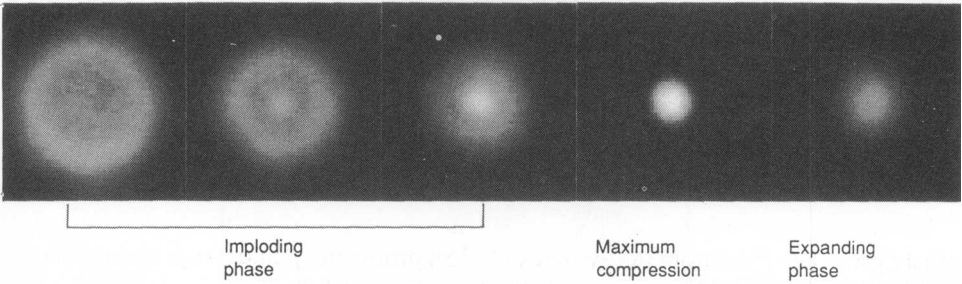phase   compression   phase

FIGURE 3   X-ray framing images of compressed target. The fourth frame corresponds to maximum compression. Frame interval 170 ps, exposure time 80 ps.

Figure 3 shows the space and time resolved x-ray images of a typical high density shot, which were taken with a multi-frame x-ray framing camera having a temporal resolution of 80 ps and responding to 1–2 keV x-rays. The maximum compression was observed at the 4th frame. The imploding shell was found to have good spherical symmetry. These framing images and x-ray streak data were compared with predictions from the 1D hydrodynamic simulation (HIMICO) as shown in Figure 4, suggesting that the implosion was nearly one-dimensional in the imploding phase. At the maximum compression phase, however, no significant information could be derived from the x-ray image because of the high x-ray opacity and the insufficient resolution of the diagnostic instrument.

The $\langle \rho R \rangle$ at the maximum compression or maximum neutron yield was measured with the Si activation technique. Figure 5 shows the γ-ray decay curve obtained from
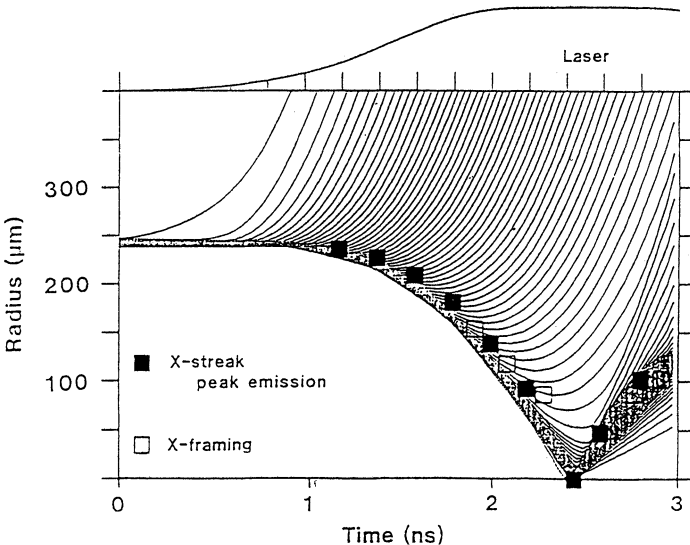

FIGURE 4   Comparison of peak x-ray emission radius with 1-d HIMICO simulation prediction.
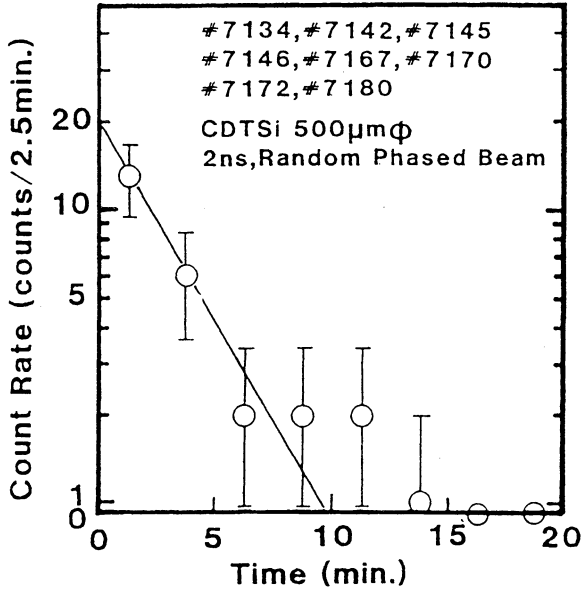
FIGURE 5   Histogram of counting signal of collected debris. Data are summed from 8 nearly identical shots for high density compression. A 2.2 min. half-life is confirmed.

several high density shots. As the number of signal counts per shot obtained $\beta-\gamma$ coincident detector was typically 2–4 counts/10 min. in these high-density shots, the data were summed over 8 identical shots. Both the decay time of 2.2 min. and the distinct spectral peak at 1.8 MeV confirmed that the detected events are really signals of ^{28}Al. In the separate implosion experiments under the same experimental conditions using a target without Si, no ^{28}Al signature was observed even when the data of 7 shots were summed. The natural background during these experiments was 0.3 counts/10 min. The background signals due to the neutron and plasma bombardments on the collector were negligibly small and at most the natural background level, respectively. Detailed analysis of the correlation between the signal counts and target uniformity showed that the target with nonuniformity of less than 1% gave more than 1 signal count in 2.2 min.

Figure 6 shows the Si activation data of $\langle \rho R \rangle$ as a function of the shell thickness. Data taken with the knock-on and secondary reaction techniques are also plotted. In the figure the error bar is mainly due to the statistical error of ^{28}Al decay signal. It is clear in Figure 6 that the $\langle \rho R \rangle$ values for the RPP case are higher by an order of magnitude than those for the normal beam case (without RPP). The high fuel areal density for the RPP case is also examined with two knock-on data points located at the knock-on limit line, indicating $\langle \rho R \rangle$ values higher than this line. In the above $\langle \rho R \rangle$ determination, we used a hot spark model where neutrons are assumed to be generated at the target center. Any other neutron distributions would result in higher $\langle \rho R \rangle$ values.

The compressed core density can be estimated from the measured $\langle \rho R \rangle$ value by
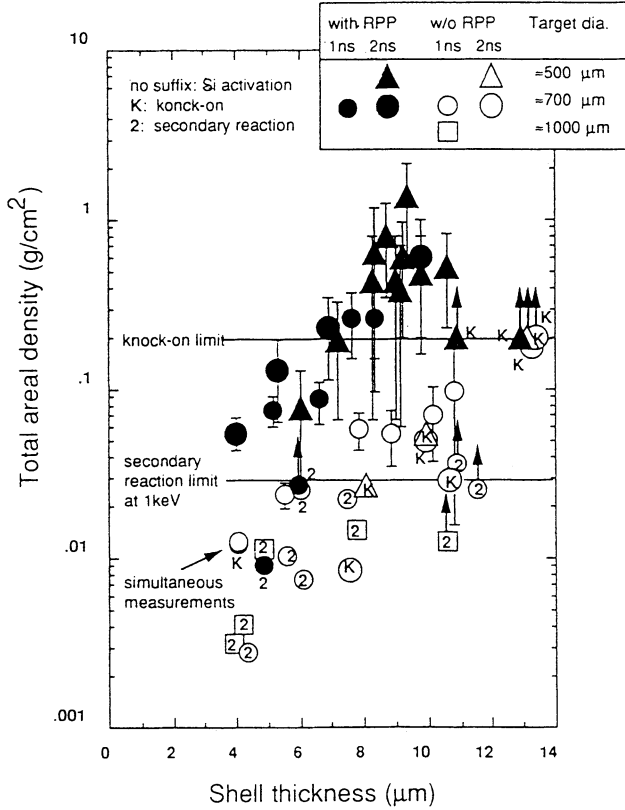
FIGURE 6   Measured fuel areal density as a function of initial shell thickness. Areal density is significantly increased with the random phase plate. Two horizontal lines shows the measured areal density limits of knock-on and secondary reaction methods.

assuming a uniform density distribution having a density ρ and radius R and using the mass conservation relation

$$\frac{4\pi}{3} \rho R^3 = M_0 - M_{abl},$$

where M_0 is the known initial mass, and M_{abl} is the ablated mass up to the maximum compression. The ablated mass was typically 0.65 M_0. This ablated mass was separately measured by using plastic shell targets coated in order, with Si, C_8H_8, Mg, and C_8H_8. The target diameter and mass were designed to be nearly the same as those for high-density experiments. The experimental results agreed well with the 1d HIMICO simulation. The agreements are convincing enough to use M_{abl} from the simulation. Uncertainty of the M_{abl} measurements results in only $\sim 10\%$ uncertainty about the fuel density.

The estimated core density is plotted in Figure 7. The average density of the 9 nearly identical shots (500 μm dia., 8–11 μm thick) was 600 g/cm³. The density of
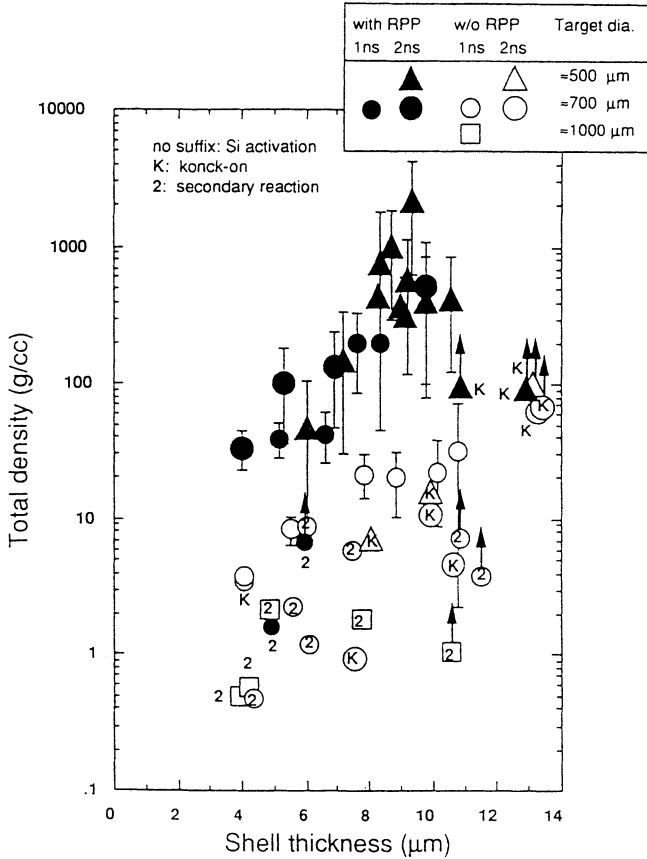
FIGURE 7   Inferred density as a function of the initial shell thickness. Average density of 9 identical shots (closed triangle points at 8–11 thickness) is 600 g/cm^3 or 600 times initial solid density.

deuterium is ~ 100 g/cm^3, i.e., $\sim 600 \times$ SD. The corresponding core radius and the convergence ratio (CR), defined as the core radius divided by the initial target radius, were estimated to be ~ 8–10 μm and 25–30, respectively. The fuel temperature was estimated from the measured neutron yields, areal densities, and fuel masses to be ~ 0.3 keV, being consistent with the measured implosion velocity and neutron time of flight method.

Although the observed areal densities were 0.6–1.2 of the predicted value from 1D simulations with convergence ratio of 25–30, the observed neutron yields were significantly lower than predictions—by three orders of magnitude. In the simulation most of neutrons were generated in the hot spark that appeared at the target center. The radius of the hot spark was calculated to be ~ 5 μm (convergence ratio of ~ 50). A possible explanation of the yield discrepancy would be that the residual non-uniformity of the implosion results in the mixing of the cold material into the hot spark region and/or resulted in insufficient conversion from the kinetic energy to the internal energy.

3.2   *Verification of Fermi Degeneracy*

The observed $600 \, g/cm^3$ hydrocarbon plasma with a temperature of 0.3 keV would be Fermi degenerated. The degenerate state could be examined with the secondary thermonuclear reaction rate. And the density of plasma could be determined if we knew the ρR and the degree of degeneracy, assuming a fully ionized plasma. In the deuterium plasma the secondary reactions are D–T and D–^{3}He reactions, where T and ^{3}He are produced by the primary D–D reaction. T and ^{3}He lose energy interacting with electrons, so the secondary reaction rate saturates in the high-ρR plasma. The saturation level is a function of electron temperature, and it increases with the temperature. However, in the degenerate plasma, the energy loss of T and ^{3}He is reduced due to quantum-mechanical effects, so the stopping range becomes longer than in non-degenerate plasma. This effect increases the secondary reaction rate if the ρR of the plasma is much larger than the stopping range of 1-MeV T and 0.8-MeV ^{3}He. That is to say, the secondary reaction rate increases with the degree of the degeneracy.

The ratio of the secondary D–T neutron yield $Y_{2nd\text{-}n}$ to the primary D-D neutron yield $Y_{1st\text{-}n}$ is calculated as a function of degree of degeneracy $\theta = k_B T/\varepsilon_F$ for CD plasmas with various electron temperatures, as shown in Figure 8, where $k_B T$ is the electron thermal energy and ε_F is the Fermi energy. Figure 9 shows the yield ratio versus the plasma density for various electron temperatures. In both figures solid and dashed curves correspond to infinite plasma and our compressed plasma, respectively. In the calculations local field correction[14], free particle polarizability[15]
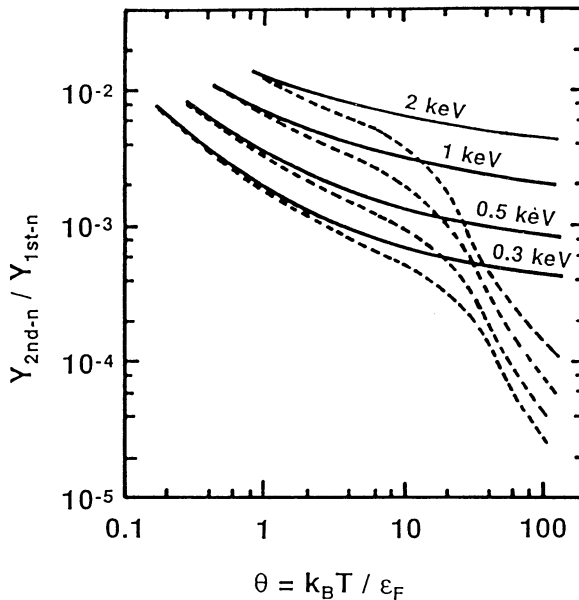

FIGURE 8   Ratio of secondary neutron yield to primary yield $Y_{2nd\text{-}n}/Y_{1st\text{-}n}$ as a function of degree of degeneracy $\theta = k_B T/\varepsilon_F$. Solid line is for infinite medium. Dashed line is for fuel plasma with a mass of 2.5×10^{-6} g which meets to the experimentally compressed CD plasma.
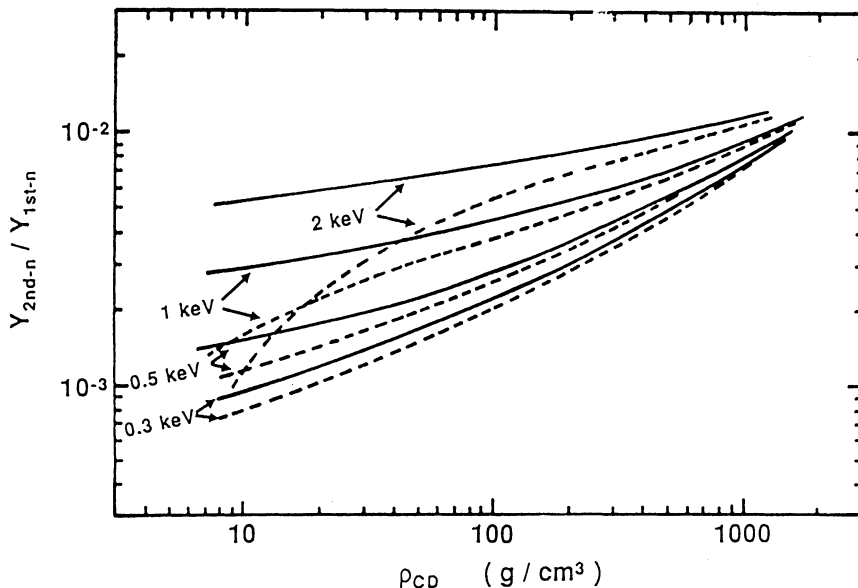
FIGURE 9   Ratio of secondary neutron yield to primary yield as a function of plasma density.

and effective ion-ion interaction potential in hyper-netted chain equation[14] were used for taking into account the short-range Coulomb interaction, Fermi degeneracy and electron shielding effects, respectively. From these figures one can decide θ, which is the measure of the degree of degeneracy, and the plasma density using the measured electron temperature and yield ratio. Note that the yield ratio should prove to be much higher than that of non-degenerate plasma using the experimentally obtained ρR and ρ.

In the experiments secondary neutron yield was measured by three plastic scintilla-tors 26 cm from the target. The background noise, which could be observed at the secondary neutron signal position on the oscilloscope trace, was carefully eliminated. The measured yield ratios are plotted as a function of the target shell thickness in Figure 10. The degree of degeneracy was plotted in Figure 11 using the calculated value (dashed curve) in Figure 8 and the measured temperature of 0.3 keV from the neutron time of flight. The degree of degeneracy was around 1 for 8–9 μm shell thickness targets. The electrons in the highly compressed plastic shell targets are partially degenerate, even assuming the electron temperature is equal to the peak ion temperature inferred from the neutron time of flight measurement. The plasma density is also estimated from Figure 9 using the yield ratio and electron temperature as shown in Figure 12, where the electron temperature was assumed to be equal to the ion temperature. The shaded region shows the plasma density measured using the neutron activation method shown in Figure 7. Note that if the electron temperature is lower than the ion temperature, the estimated density increases. The error bars in Figures 10 to 12 are mainly due to the statistical error of the yield ratio. The density
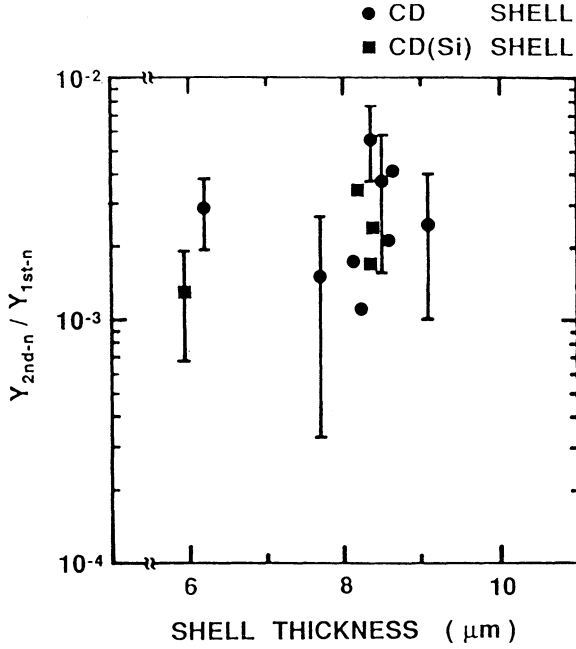
FIGURE 10   Experimentally observed Y_{2nd-n}/Y_{1st-n} as a function of target shell thickness.
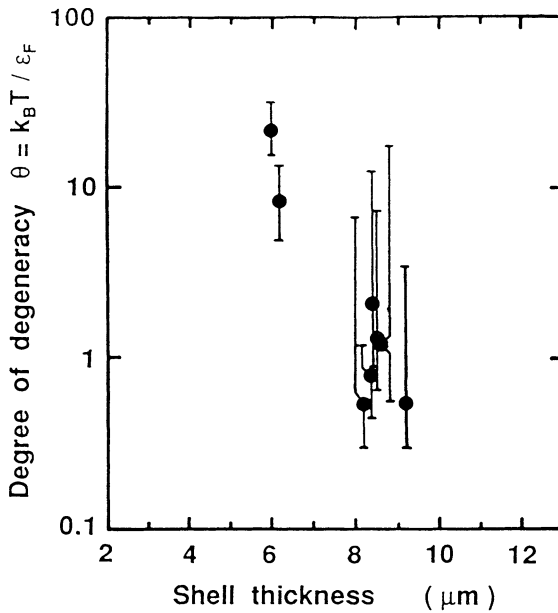

FIGURE 11   Inferred degree of degeneracy as a function of target shell thickness. Partially degenerate plasma, $\theta \sim 1$, are observed in the implosion of 8–9-μm thick targets.
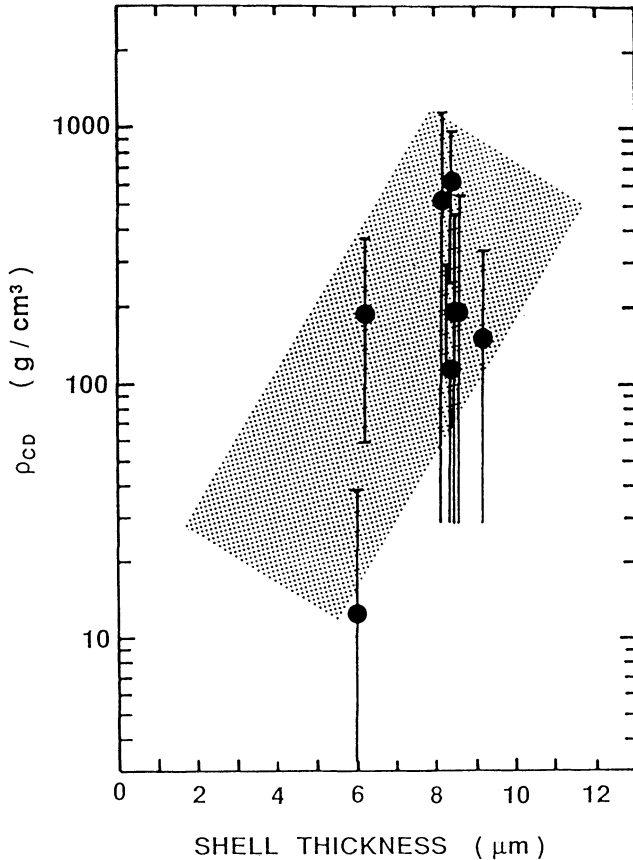
FIGURE 12   Inferred plasma density as a function of target shell thickness. Shaded region shows the density measured with the neutron activation method.

inferred by the yield ratio of the secondary to the primary neutrons yield was 600 g/cm^3, which was consistent with the results obtained from the activation measurements.

4   SUMMARY

High density compression of 600 × the solid density was demonstrated with high-quality deuterated hydrocarbon-shell targets. A Fermi degenerate state in high temperature laboratory plasma has been observed by means of the secondary reaction rate measurements. Those results are owed to the improvement of laser illumination uniformity with a random phase plate; introduction of high-quality plastic-shell targets; and establishment of the neutron activation and secondary reaction techniques for ρR diagnostics.

REFERENCES

1. J. D. Kilkenny, *et al.*, *Plasma Physics and Coantrolled Nuclear Fusion Research 1988*, Vol. 3 (IAEA, Vienna, 1988) p. 26.
2. F. Ze, Lawrence Livermore National Laboratory Report, UCRL-50021-84 (1985) pp. 5–35.
3. R. L. McCrory, *et al.*, *Nature* **335**, 225 (1988).
4. S. Nakai, *et al.*, *Plasma Physics and Controlled Nuclear Fusion Research 1988*, Vol. 3, (IAEA, Vienna, 1988) p. 3.
5. Y. Kato, *et al.*, *Phys. Rev. Lett.* **53**, 1057 (1984).
6. T. Yabe, *et al.*, *Nucl. Fusion* **21**, 803 (1981). Recently, HIMICO was improved to treat nonlocal heat transport with the Fokker-Plank equation.
7. M. Takagi, *et al.*, *J. Vac. Sci. Tech.* **A9**, 2145 (1991).
8. H. Nakaishi, doctoral thesis, Osaka University (Osaka, Japan, 1990).
9. H. Azechi, *et al.*, *Appl. Phys. Lett.* **49**, 555 (1986).
10. S. Kacenjar, *et al.*, *Appl. Phys. Lett.* **49**, 463 (1982).
11. H. Nakaishi, *et al.*, *Appl. Phys. Lett.* **54**, 1308 (1989).
12. M. E. Cambell, *et al.*, *Appl. Phys. Lett.* **36**, 965 (1980).
13. H. Nakaishi, *et al.*, *Appl. Phys. Lett.* **55**, 2072 (1989).
14. S. Ichimaru, *et al.*, *Phys. Rev. A* **32**, 1768 (1985).
15. C. Khanna and H. R. Glyde, *Can. J. Phys.* **54**, 648 (1976).